



Tin-embedded carbon nanofibers as flexible and freestanding electrode materials for high-performance supercapacitors

Jing Liu¹ · Xingwei Sun¹ · Chunping Li¹ · Jie Bai¹

Received: 31 January 2019 / Revised: 8 April 2019 / Accepted: 15 April 2019 / Published online: 23 May 2019
© Springer-Verlag GmbH Germany, part of Springer Nature 2019

Abstract

Tin carbon nanofibers were prepared by electrospinning and carbonization as flexible and independent supercapacitor materials. Sn/CNFs, Sn/SnO/CNFs, and SnO₂/CNFs were prepared by different carbonization processes. The specific capacitances at 0.5 A g⁻¹ were 761.39 F g⁻¹, 712.29 F g⁻¹, and 589.78 F g⁻¹, respectively. The composite nanofibers were characterized by SEM, XPS, TEM, XRD, and Raman spectroscopy. It was found that tin nanoparticles were well dispersed in carbon nanofibers and no aggregated crystalline phase was formed. These results showed that Sn/CNFs was superior to Sn/SnO/CNFs and SnO₂/CNFs in electrochemical performance of supercapacitors. In addition, a very stable cycle stability had been achieved. Even after 10,000 charge-discharge cycles, Sn/CNFs still maintain excellent specific capacitance of up to 114% of its initial performance. Moreover, Sn/CNFs//CNFs was assembled as a flexible all-solid-state asymmetric supercapacitor (ASC) with the energy density of 57.18 Wh kg⁻¹ at a power density of 374.97 W kg⁻¹.

Keywords Carbon nanofibers · SnO_x · Valence state · Supercapacitor

Introduction

Continuing growth in fossil energy consumption causes great environmental challenges and stimulates clean, sustainable energy research [1, 2]. Supercapacitors (SCs), as a new sort of energy storage device, provided the most promising method to store electricity on account of their unique merits of fast power release and long-term stability [3, 4]. According to energy storage mechanism, SCs are divided into two primary types. The first one depends upon the electrochemical double-layer capacitance (EDLC), where the energy storage and delivery are carried out by electrode-electrolyte interface [5]. Although this type of SCs has a high power density and splendid cycling stability, the low energy density is limited by double-layer superficial area. The other depends on invertible Faradaic reaction on the electrode materials, which is called pseudocapacitors. According to the report, the redox-active materials could offer a specific capacitance that exceeds 10

times that of carbon-based EDLC [6]. Therefore, the study of pseudocapacitors is very promising.

However, the performance of pseudocapacitors depends closely on the physicochemical properties of their electrode materials [7]. Hence, the main direction of the study has paid close attention in exploring alternative pseudocapacitance electrode materials. SnO_x, as a N-type semiconductor, which possesses a wide energy gap (E_g = 3.62 eV, at 300 K), is nontoxic, inexpensive, and widely available [8]. In addition, SnO_x is a very attractive candidate for efficient electrochemical energy storage system because of its characteristic physicochemical properties, such as cycling stability [9], whereas the usability of SnO_x is limited due to its low electrical conductivity [10]. In addition, the aggregation of SnO_x nanoparticles and large volume expansion, which brings about mechanical breakdown and poor electric contact between the collector and electrode, also restrict the cycle stability and cause big capacity fading [11–13]. There are two strategies to solve the above problems: (i) control the particle size of SnO_x, including fabricating nano-sized SnO_x [14–17] and (ii) dope SnO_x into the carbon material to form SnO_x-carbon composites. Nanomaterials are ideal candidates as electrode materials owing to them providing favorable electronic transmission capability and high surface to volume ratio [18]. By reducing the SnO_x particle size to atomic level, all tin in the

✉ Chunping Li
hgcp_li@126.com

¹ Chemical Engineering College, Inner Mongolia University of Technology, Inner Mongolia Key Laboratory of Industrial Catalysis, Hohhot 010051, People's Republic of China

SCs might become electrochemically active, thereby significantly improving specific capacitance. In another regard, active carbon including graphene, carbon nanofibers (CNFs), and carbon nanotubes (CNTs) show higher electrical conductivities, but the inherent shortcoming is their low storage capacity and the poor traits of low specific capacitance [19–22]. Furthermore, carbon-based materials do not merely provide an effective buffer to reduce the volume change of SnO_x but as a conductive phase, carbon-based materials make up for the low conductivity of SnO_x . Therefore, it is an effective strategy to combine SnO_x with carbon materials so that they can play a synergistic role [23, 24].

Recent studies showed that nickel foam, nickel foil, and carbon cloth were used as collector to enhance the whole electroconductivity [25]. Moreover, because conductive additives and binder are employed on a current collector, achieving the portable equipment with light quality and small volume is difficult. On the other part, the unreactiveness binders attached to the electrode will lead to the decay of electron conductivity [26–30]. Accordingly, it is considered that the development without adhesive self-supported electrodes in electrochemical energy devices is extremely required.

In addition, valence state has been proved to be an important factor affecting the electrochemical performance of supercapacitors. For instance, Zhao et al. reported that vertically aligned MnO_2 nanosheets coupled with carbon nanosheet composite electrode were applied in supercapacitors, in which the specific capacitance of MnO/CNS and MnO_2/CNS at 0.5 A g^{-1} were 180.2 F g^{-1} and 339 F g^{-1} [31]. Very recently, Kumar et al. reported the single-step solvothermally synthesized CeO_2 nanoparticles applied in supercapacitors, in which the specific capacitances of $\text{CeO}_2@20\text{h}$ (29% Ce^{3+} , 71% Ce^{4+}) and $\text{CeO}_2@10\text{h}$ (15% Ce^{3+} , 85% Ce^{4+}) at 0.25 A g^{-1} were 143 F g^{-1} and 90 F g^{-1} [32]. Furthermore, the Ki group reported that the specific capacitance values of electrodes containing $\text{Cu}^{0+}/\text{Cu}^{1+}$ and the specific capacitance of $\text{Cu}^{1+}/\text{Cu}^{2+}$ are 22.8 F g^{-1} and 24.3 F g^{-1} , respectively [33]. Moreover, Huang et al. reported the effect of vanadium in different valence states on specific capacitance and confirmed that $\text{V}_2\text{O}_5/\text{CFs}$ (606 F g^{-1}) is better than that of $\text{V}_2\text{O}_3/\text{CFs}$ (460 F g^{-1}) and $\text{VO}_2\text{-V}_2\text{O}_5/\text{CFs}$ (476 F g^{-1}) at 0.5 A g^{-1} when applied in supercapacitor [34]. It is worth noting that tin also has multiple oxidation states (Sn^0 , SnO , SnO_2), but the effects of different valences of tin applied in supercapacitors have been rarely reported.

Herein, the electrospinning and carbonization method was used to prepare the different proportions of SnCl_2/PAN , and study its effect on the properties of supercapacitors. Under the optimal proportion, by changing different carbonization conditions to obtain different valence states of tin, they were Sn/CNFs , $\text{Sn}/\text{SnO}/\text{CNFs}$, and SnO_2/CNFs , respectively. In this work, we hope that the reversible reaction of SnO_x/CNFs electrode can be

optimized during charging and discharging by adjusting the different doping amounts and valence states of tin, so as to enhance the performance of supercapacitors [35].

Experimental section

Materials

Polyacrylonitrile (PAN, $M_w = 80,000$) was supplied by KunshanHongyu Plastics Co., Ltd. N, N-Dimethylformamide (DMF, AR, 99.5%) was furnished by Tianjin Fuyu Fine Chemical Co., Ltd. Tin (II) chloride dehydrate ($\text{SnCl}_2 \cdot 2\text{H}_2\text{O}$, GR, 98%) was purchased from Tianjin Rujint Chemical Co., Ltd. Potassium hydroxide (KOH, GR, 99.5%) was from Sinopharm Chemical Reagent Co., Ltd. All reagents applied were of analytical grade and used directly without any depuration.

Synthesis of different ratios of tin-embedded carbon nanofibers

The synthetic process for preparing different ratios of SnO_x -embedded carbon nanofibers is described as follows. 7.5 wt% PAN was dissolved in DMF, which was constantly stirred for 24 h at room temperature. And $\text{SnCl}_2 \cdot 2\text{H}_2\text{O}$ was dissolved in this PAN/DMF solution; the mixture was stirred for 24 h at $25 \text{ }^\circ\text{C}$ to form a well-distributed solution. Afterwards, the well-distributed mixing solution was named SnCl_2/PAN solution. The solution was kept in a spinning nozzle with the distance between the needle and collector of 20 cm and the working pressure in the electrospinning system of 15 kV. In an effort to identify an optimized composition, different amounts of $\text{SnCl}_2 \cdot 2\text{H}_2\text{O}$ were dissolved into the PAN solution. The molar ratio of acrylonitrile (AN) to $\text{SnCl}_2 \cdot 2\text{H}_2\text{O}$ was 10, 20, 30, 40, and 50, respectively. Then, the film was stabilized at $220 \text{ }^\circ\text{C}$ for 2 h at air atmosphere and carbonized at $500 \text{ }^\circ\text{C}$ for 2 h in a nitrogen atmosphere in a tube furnace. And the samples were labeled SnO_x/CNFs (10), SnO_x/CNFs (20), SnO_x/CNFs (30), SnO_x/CNFs (40), and SnO_x/CNFs (50), respectively.

Synthesis of different valence states of tin-embedded carbon nanofibers ($\text{SnO}_2\text{-CNFs}$, $\text{Sn}/\text{SnO}/\text{CNFs}$, and Sn/CNFs) (Scheme 1)

Preparation of $\text{SnO}_2\text{-CNFs}$: SnCl_2/PAN films were heated 2 h at $220 \text{ }^\circ\text{C}$ in air atmosphere; the heating rate began at room temperature of $5 \text{ }^\circ\text{C}/\text{min}$ in a tube furnace to increase the stability of PAN [36] and further annealed at $500 \text{ }^\circ\text{C}$ for 2 h in N_2 .

Preparation of Sn/SnO/CNFs: SnCl₂/PAN films were heated 2 h at 220 °C; the heating rate began at room temperature of 5 °C/min and further annealed at 600 °C for 3 h. The whole process was performed under N₂.

Preparation of Sn/CNFs: SnCl₂/PAN films were heated 2 h at 220 °C; the heating rate began at room temperature of 5 °C/min and further annealed at 700 °C for 3 h. The whole process was performed under N₂.

Characterization

The microstructure of the SnO_x/CNFs was investigated by scanning electron microscopy (SEM, Pro, Phenom, Netherlands), and transmission electron microscope (TEM, F20 S-TWIN, Tecnai). The valence states of tin were investigated by X-ray photoelectron spectroscopy (XPS, Escalab 250xi, Thermo Fisher Scientific USA). X-ray diffraction (XRD, SmartLab 9 KW, Japan) was used to study the crystalline structures of the mats over a range of 2θ angles from 10° to 80° at a scanning rate of 10°/min. Raman spectra (InVia Microscope Raman, Renishaw, England) was recorded with an argon laser (λ = 532 nm) excitation source. The tin content was measured by the inductively coupled plasma-optical emission spectroscopy (ICP-OES 730, Agilent, USA) instrument. The specific surface area of the samples were measured with a Micromeritics ASAP 2020 analyzer.

Electrochemical measurement

For the three-electrode electrochemical tests, the electrochemical performance of SnO_x/CNFs was detected by cyclic voltammetry (CV), galvanostatic charge-discharge (GCD), and electrochemical impedance spectroscopy (EIS) in a three-electrode system in 4 mol/L KOH at room temperature. Pt mesh and Hg/HgO electrode were used for the counter electrode and the reference electrode, individually. In this process, SnO_x/CNFs (0.7 mg/cm²), which were placed in the middle of two nickel foams at the pressure of 10 MPa on the table press for about 60 s, were used for the working electrode without conductive additive or binder. The specific capacitance (C, F/g) in the three-electrode collocation can be calculated in accordance with the following equality:

$$C = \frac{I \times \Delta t}{m \times \Delta V} \quad (1)$$

where I (A) is the discharge current, Δt (s) is the discharge time, m (g) is the mass of the electrode, and ΔV (V) is the potential charge during the discharge time after IR drop. The whole electrochemical performance was achieved by using CHI660E electrochemical work-station (Chenhua, Shanghai).

For the two-electrode electrochemical tests, an asymmetric supercapacitor was successfully assembled employing the Sn/

CNFs composite as the positive electrode and carbon nanofibers-700 °C (CNFs-700) as the negative electrode. The positive and negative materials were placed in the middle of the foam nickel and pressed at 10 MPa for about 60 s to form a sandwich structure to obtain positive and negative electrodes. Before assembling, the electrodes were immersed in KOH electrolyte overnight. According to the charge balance mechanism, the mass of active materials on positive and negative electrodes was calculated by formula (2). Specific capacitance (C), energy density (E), and power density (P) are calculated according to the following formulas (3)–(5):

$$\frac{m_+}{m_-} = \frac{C_- \times \Delta V_-}{C_+ \times \Delta V_+} \quad (2)$$

$$C = \frac{I \times \Delta t}{M \times \Delta V} \quad (3)$$

$$E = \frac{1}{2} C \Delta V^2 \quad (4)$$

$$P = \frac{E}{\Delta t} \quad (5)$$

in which m_+/m_- (mg) represents the mass of the positive and negative electrodes respectively, C_+/C_- (F g⁻¹) and ΔV (V) represents the specific capacitance and potential windows of the two electrodes. M (mg) is the total mass of the two electrodes. In addition, Δt (s), E (Wh kg⁻¹) and P (W kg⁻¹) represent discharge time, energy density, and power density, respectively.

Results and discussion

Effect of SnCl₂/PAN ratio on supercapacitor performance

To explore the optimal ratio of SnCl₂ to PAN, the electrochemical properties of SnO_x/CNFs (10), SnO_x/CNFs (20), SnO_x/CNFs (30), SnO_x/CNFs (40), and SnO_x/CNFs (50) were investigated using cyclic voltammetry (CV), galvanostatic charge-discharge (GCD), and electrochemical impedance spectroscopy (EIS). The films possess good mechanical strength and flexibility, while the carbon-rich properties of nanofibers ensure high conductivity. Accordingly, the films enable to be directly used as electrode materials for supercapacitors without any conductive additive or binder. The CV curves of different proportions at the scan rate of 70 mv s⁻¹ with the potential window of 0–0.65 V (Fig. 1), and SnO_x/CNFs (40) exhibited the largest induced current among all samples. The CV curves have evident redox peaks, which attested that the capacitance behavior was mainly Faraday pseudocapacitance produced by reversible redox reaction. Moreover, the GCD curves of SnO_x/CNFs in the potential range of 0–0.53 V at current density of 0.5 A g⁻¹ are shown in Fig. 2. SnO_x/CNFs present distinct plateau region, which expresses that the samples have good activity of redox reaction. According to

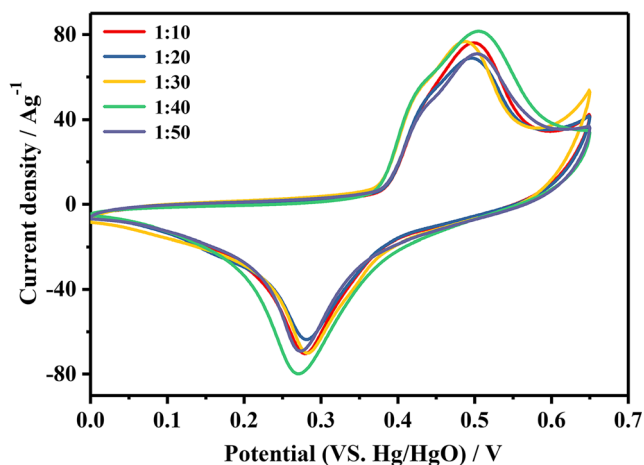


Fig. 1 CV curves of SnO_x/CNFs (10), SnO_x/CNFs (20), SnO_x/CNFs (30), SnO_x/CNFs (40), and SnO_x/CNFs (50) at a scan rate of 70 mV s⁻¹

the calculation and drawing of specific capacitance in Fig. 3, the composite electrode SnO_x/CNFs (40) delivered the highest specific capacitance of 589.78 F g⁻¹ at 0.5 A g⁻¹. The corresponding specific capacitances were 506.70, 514.77, 520.81, and 532.47 F g⁻¹ for the SnO_x/CNFs (10), SnO_x/CNFs (20), SnO_x/CNFs (30), and SnO_x/CNFs (50), respectively. As the current density increases from 0.5 to 5 A g⁻¹, during the oxidation-reduction transition of tin oxide, the specific capacitance decreases gradually due to proton dissipation and the significant reduction of ionic conductivity in the electrolyte. To further evaluate the properties of the samples, Fig. 4a and b show the results of their resistance tests. The electrode resistance of SnO_x/CNFs (40) (0.454 Ω) is lower than SnO_x/CNFs (10) (0.484 Ω), SnO_x/CNFs (20) (0.486 Ω), SnO_x/CNFs (30) (0.487 Ω), and SnO_x/CNFs (50) (0.489 Ω). Comprehensive electrochemical tests show that the optimal molar ratio between PAN and tin is 40/1.

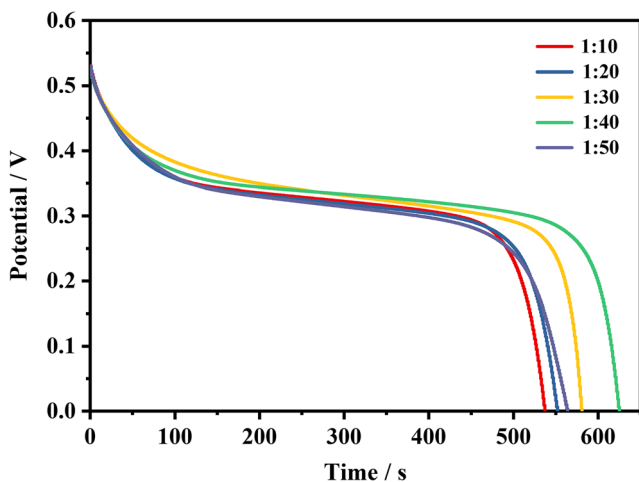


Fig. 2 Charge and discharge curves of SnO_x/CNFs (10), SnO_x/CNFs (20), SnO_x/CNFs (30), SnO_x/CNFs (40), and SnO_x/CNFs (50) at a current density of 0.5 A g⁻¹

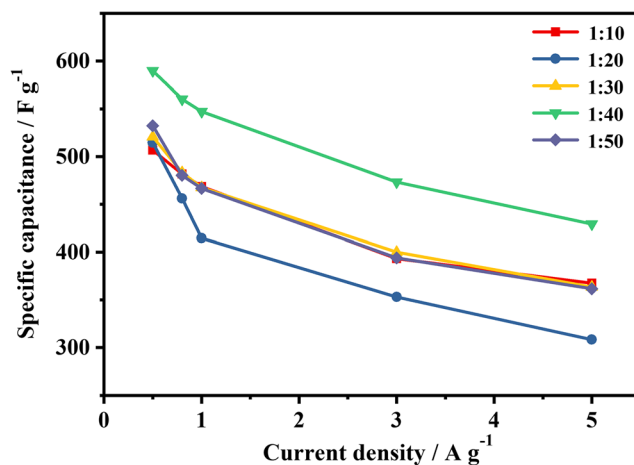


Fig. 3 Specific capacitance of SnO_x/CNFs (10), SnO_x/CNFs (20), SnO_x/CNFs (30), SnO_x/CNFs (40), and SnO_x/CNFs (50) at different current densities

Effect of Sn valence states on the performance of supercapacitors

At different carbonization temperatures, the valence state of tin changes significantly. Herein, the effects of Sn⁰, Sn²⁺, and Sn⁴⁺ on the relative capacitance were further investigated. The morphology characterization of composite nanofibers was estimated by scanning electron microscopy (SEM). The SEM images of synthesized fibers are shown in Fig. 5, in which the surface of the fibers are very smooth and no tin atoms particles accumulate on the surface of the fibers. The result indicates the tin atoms particles are embedded in the fibers. The aggregation of tin-related crystalline phase was not obviously observed, which further reveals that the tin employed in this study is well dispersed within the nanofibers. And the diameters range from 303 to 168 nm. During the carbonization process, the diameter of the fiber shrinks but still maintains its original appearance. It is speculated that the second step high-temperature carbonization process brings about the complete decomposition of PAN. Furthermore, the composite carbon fibers have high flexibility even under high-temperature annealing.

In order to better understand the surface composition of the composite nanofibers, especially the valence state of tin in the different carbonization processes, XPS was employed. The XPS survey spectra in Fig. 6a reveals the sample with carbonization temperature of 500 °C, which consist of carbon, oxygen, nitrogen, and tin atoms. The peaks at 286, 398, 495, and 530.5 eV are attributed to C 1s, N 1s, Sn 3d_{5/2}, and O 1s, separately. The C 1s spectrum is segmented into four peaks (Fig. 6a-C). The peaks at 284.4 eV, 285.4 eV, 286.3 eV, and 288.9 eV are assigned to C-C, C-N, C-O, and C=O [37]. The N 1s spectrum is divided into two peaks (Fig. 6a-N); the peaks at 399.7 eV and 397.9 eV are attributed to the pyrrolic N and pyridinic N, respectively. The O 1s spectra (Fig. 6a-O) can be

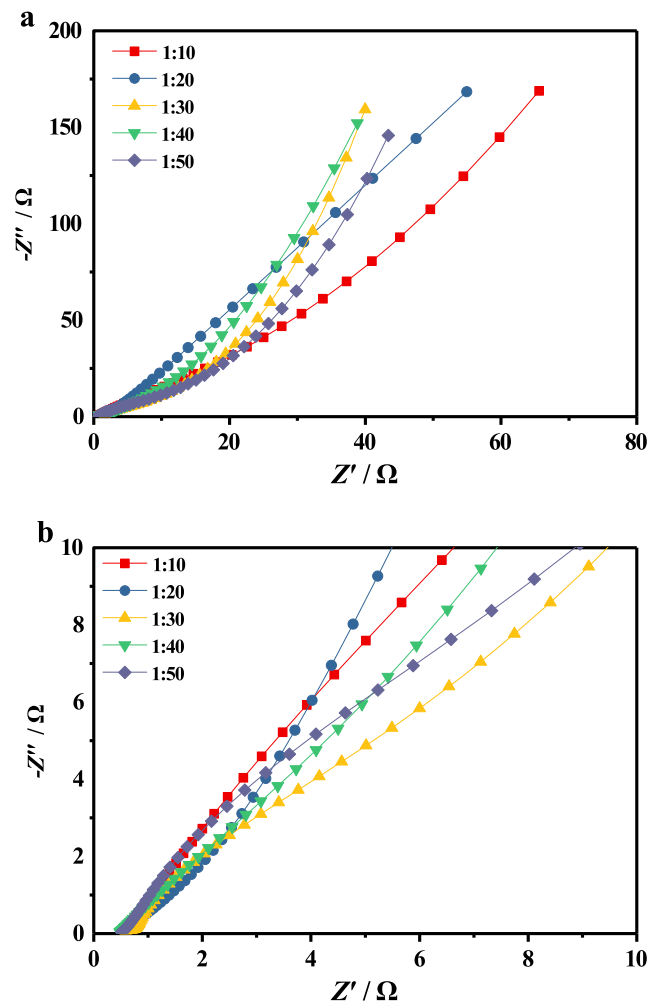


Fig. 4 (a) Nyquist plots of SnO_x/CNFs (10), SnO_x/CNFs (20), SnO_x/CNFs (30), SnO_x/CNFs (40), and SnO_x/CNFs (50), (b) magnified version of the Nyquist plots

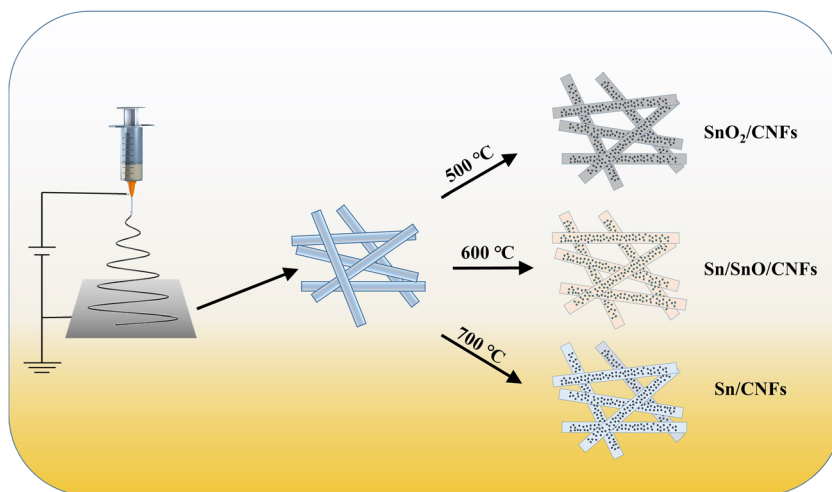
assigned of Sn–O (530.4 eV), C=O (531.4 eV), OH[−] (532.1 eV), C–O (533.6 eV), and H₂O (532.5 eV) [38]. The high-resolution Sn spectrum in Fig. 6a shows Sn 3d_{5/2} and Sn 3d_{3/2} peaks; the peak-to-peak separation energy is 8.5 eV, indicating that the tin in the compound was in the Sn⁴⁺ oxidation state [8]. Accordingly, the sample is labeled SnO₂/CNFs. What's more, the sample with carbonization temperature of 600 °C, the Sn 3d peak is fitted by two peaks (Fig. 6b–Sn), corresponding to metallic Sn (485.3, 493.7 eV) and Sn²⁺ (486.3, 494.8 eV), indicating that the tin in the compound was the existence of Sn²⁺ mixed with metallic Sn. The sample is labeled Sn/SnO/CNFs. In addition, in the sample with carbonization temperature of 700 °C, Sn 3d_{5/2} and Sn 3d_{3/2} peaks at 485.3 eV and 493.7 eV (Fig. 6c–Sn), which proved that metallic Sn exists in the carbonization temperature of 700 °C. The sample is labeled Sn/CNFs.

Sn/CNFs was also characterized by TEM and HR-TEM to acquire further information related to the microstructure of nanofibers. The diameter of Sn/CNFs is around 150 nm after calcining at high temperature (Fig. 7a). Figure 7 b and c are

representative HR-TEM images of single nanofibers. However, the TEM inspection did not observe the metallic Sn lattice even after increasing higher magnifications. Through observation, tin element was found to be well dispersed in the carbon nanofibers, free from the formation of an aggregated crystalline phase, sustaining the amorphous nature of the composite consistent with the results from the XRD. Figure 8 shows the consequence of elementary substance mapping, which distinctly indicates the presence of C, N, and Sn well-distributed along the CNFs. The uniform distribution of elements enhances the conduct of electrode materials with ions. The tin content in Sn/CNFs composite was determined by ICP-OES. The result showed the amount of tin was 8.06 wt%.

In order to inspect the phase composition, the Sn/CNFs was measured by XRD, which was shown in Fig. 9. The broad peak at 25° and 43° corresponds to the (002) and (100) diffraction planes of graphite, respectively, and reveals the existence of carbon. No peaks are observed for different phases of tin (Sn, SnO, SnO₂, etc.). The XRD results further confirm the

Scheme 1 Schematic illustration of the fabrication steps for different valence states of amorphous tin based on carbon nanofibers



amorphous metallic tin, which agrees well with the TEM images. These results illustrate amorphous tin in the sample. Amorphous metallic tin has better capacitive properties. This

is because, in an amorphous metallic tin composite, in atomic specifications, tin is bonded to the carbon skeleton by a covalent bond, which promotes the conduction and contact of metals with electrons and electrolyte ions, so that the samples have excellent electrochemical property.

In order to investigate the vibration performance of the SnO_x/CNFs samples carbonized at sundry conditions, the characterization of Raman spectrum has been employed and Fig. 10 shows the Raman spectrum of Sn/CNFs , $\text{Sn}/\text{SnO}/\text{CNFs}$, and SnO_2/CNFs . The peaks at 1590 and 1357 cm^{-1} are attributed to the intra-plane vibration pattern of Raman active E_{2g} and intra-plane respiratory vibration pattern of Raman inactive A_{1g} , respectively, known as G (graphite) and D (disordered) bands. The existence of these bands indicates that the organic substances in the films experienced decomposed and converted into solid carbon after the calcination process. The results of Raman spectroscopy are according to those of XRD results. In addition, no adsorption bands corresponding to the Sn phases were observed within the spectral range. The absence of absorption band reveals that there is no Sn aggregate in the films. The relative intensity proportion of the D-to-G-bands is the R value, which reveals the degree of graphitization and alignment of the graphitic plane. Lower R value corresponds to higher amount of sp^2 (graphite) clusters [39]. In this work, Sn/CNFs , $\text{Sn}/\text{SnO}/\text{CNFs}$, and SnO_2/CNFs have R values of 1.47, 1.27, and 1.15, respectively. From these ratios, it can be seen that the graphitization process of metallic tin with different valence states has no prominent change. However, with the increase of metallic tin, it shows a slightly lower degree of graphitization, indicating that the degree of graphitization of carbon is inhibited by metallic tin.

The nitrogen adsorption/desorption isotherm of the sample SnO_2/CNFs , $\text{Sn}/\text{SnO}/\text{CNFs}$, and Sn/CNFs are shown in Table. 1. By comparison, the specific surface area of the $\text{Sn}/$

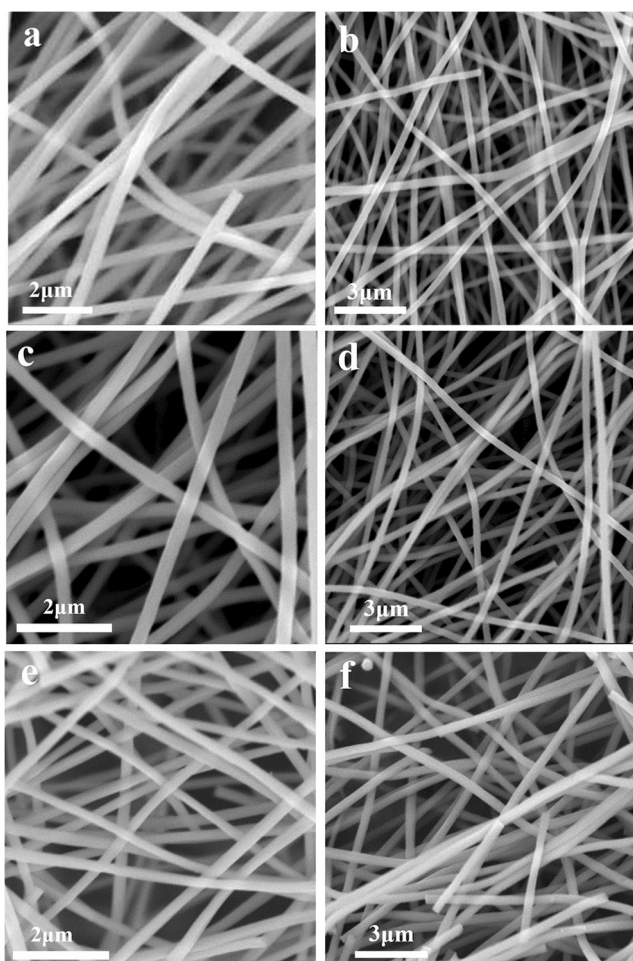


Fig. 5 SEM images of samples with different carbonization temperatures of (a–b) $500\text{ }^\circ\text{C}$, (b–d) $600\text{ }^\circ\text{C}$, (c–f) $700\text{ }^\circ\text{C}$

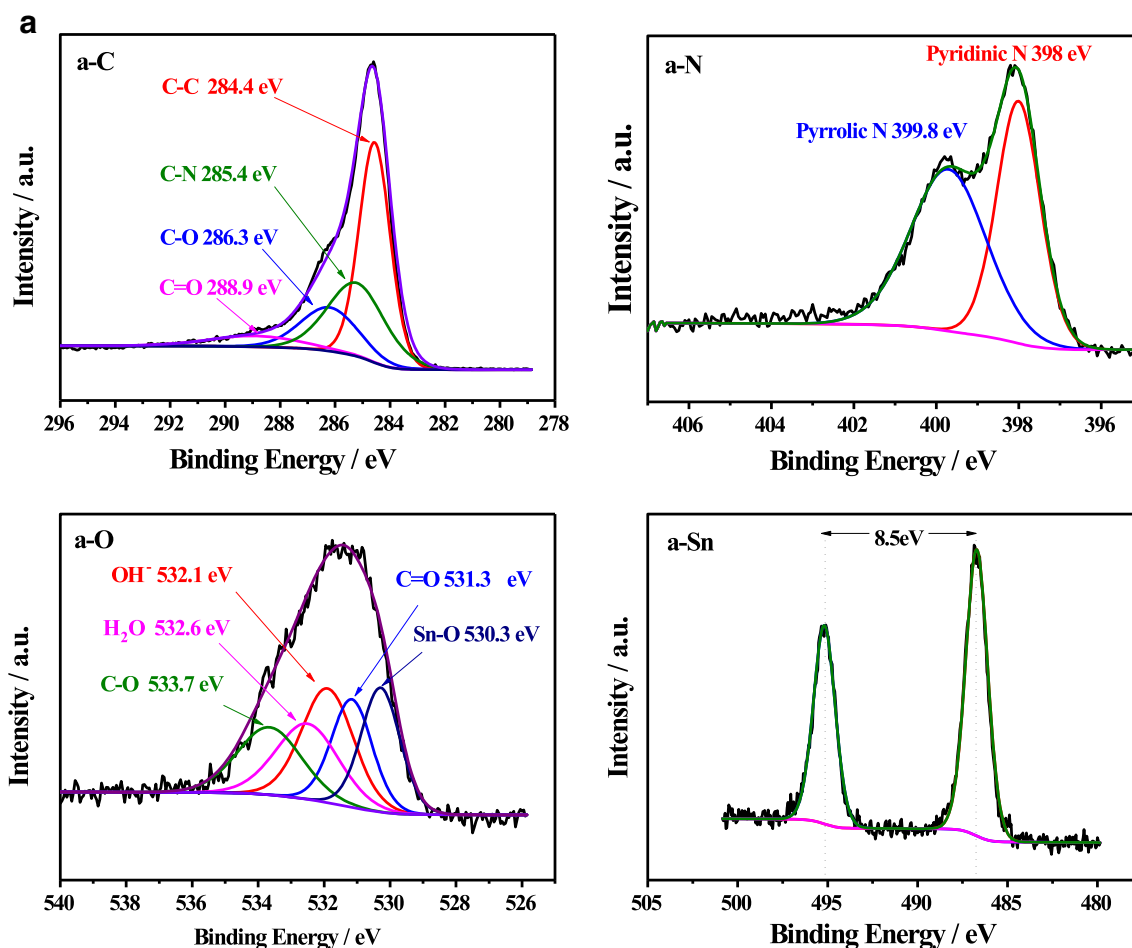


Fig. 6 XPS spectrum of (a) SnO_2/CNFs , (b) $\text{Sn}/\text{SnO}/\text{CNFs}$, (c) Sn/CNFs

CNFs composite is $24.65 \text{ m}^2 \text{ g}^{-1}$, which is higher than that of $\text{Sn}/\text{SnO}/\text{CNFs}$ ($23.62 \text{ m}^2 \text{ g}^{-1}$) and SnO_2/CNFs ($20.27 \text{ m}^2 \text{ g}^{-1}$). These pores provide a low resistance channel for ion exchange between electrodes and electrolytes and improve the electrochemical performance [40].

The TGA of SnO_2/CNFs , $\text{Sn}/\text{SnO}/\text{CNFs}$, and Sn/CNFs was offered, as shown in Fig. 11. The thermogravimetric test procedure is basically consistent with the carbonization procedure and atmosphere for preparing Sn with different valences. In Fig. 11A, during the first step (50–220 °C), 7.22% of the weight loss in the first stage is attributed to the evaporation of water adsorbed on the surface. When keeping at 220 °C for 1 h, the weight has remained almost unchanged. After N_2 filling, PAN was completely decomposed (24.43%) from 220 to 500 °C. Finally, the residuals of Sn and carbon are about 68.35%. The second carbonization process is carried out in N_2 atmosphere (Fig. 11B), during the first step from about 50 to 220 °C, 4.44% is attributed to the release of water, when keeping 1 h at 220 °C, the weight has remained almost unchanged. The second loss step is attributed to the complete decomposition of PAN (17.65%), and the final 1.99% weight loss is due to the

reduction of Sn by carbon. The carbonization of Sn/CNFs was carried out in N_2 atmosphere (Fig. 11C). The weight loss in the first stage is attributed to evaporation of water (9.34%) and no significant change in the sample weight for 1 h at 220 °C. The second weight loss is due to the complete decomposition of PAN (19.85%). The weight loss ascribed to carbon reduction is 7.33%, and the final residual Sn and C are 60.66%. The process of Sn reduction by carbon can be observed in the figures, which explain the formation of metallic Sn.

The electrochemical performance of SnO_2/CNFs , $\text{Sn}/\text{SnO}/\text{CNFs}$, and Sn/CNFs were estimated via cyclic voltammetry (CV) and galvanostatic charge-discharge measurement (GCD). Figure 12 shows the cyclic voltammetric (CV) curves of the samples at the scan rate of 70 mv/s with typical oxidation-reduction peaks in a potential window of 0–0.65 V. The peaks in the CV curves reveal the existence of the Faradaic reaction in the tin-containing composite. Among all samples, Sn/CNFs has brought out the largest current response along with the maximum integral area of the CV curves, revealing the maximum pseudocapacitance [41]. The CV curve of Ni foam was also recorded. The image shows a

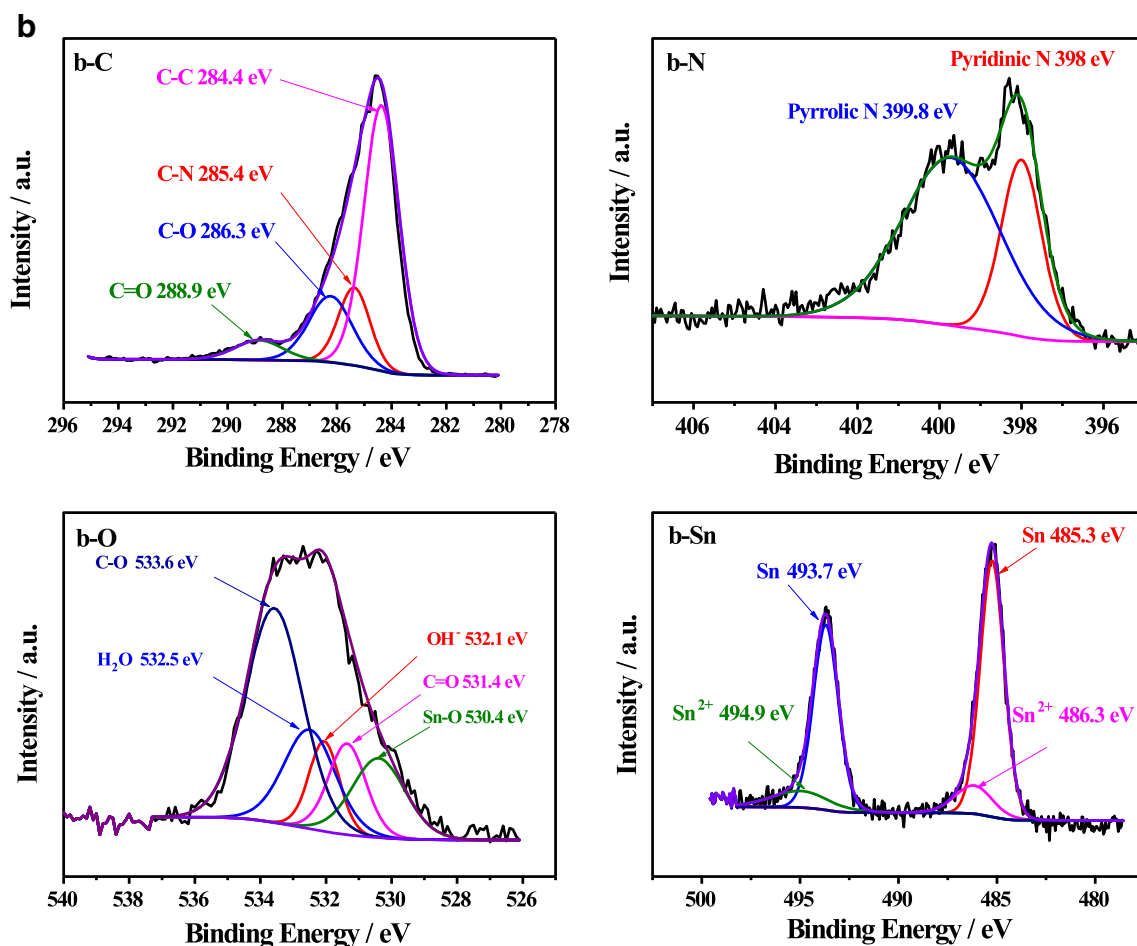


Fig. 6 (continued)

very weak peak, indicating that the effect of Ni foam can be neglected.

The capacitance characteristics were further tested using galvanostatic charge-discharge (GCD) measurements (Fig. 13). Every last GCD curve has electric voltage platform that fully conforms to the typical redox peak in CV curves in the voltage window of 0–0.53 V, and the current density was immobilized at 0.5 A g⁻¹. Discharge time of composite materials with Sn/CNFs was longer than other samples at the equal current density and active material quality. The samples deliver capacitances of 589.78 F g⁻¹, 712.29 F g⁻¹, and 761.39 F g⁻¹ for SnO₂/CNFs, Sn/SnO/CNFs, and Sn/CNFs, respectively. It can be seen from the capacitance data that, as the tin valence state increases, the specific capacitance value gradually decreases. In conclusion, the Sn/CNFs has a higher capacitance value than that of the others. In addition, after reading many related literatures [42, 43], we proposed a possible energy storage mechanism of Sn/CNFs:

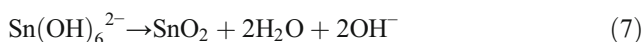


Figure 14 a–e show the CV curves of three different types of electrode materials at different scanning rates from 2 to 70 mV s⁻¹. For SnO₂/CNFs, Sn/SnO/CNFs, and Sn/CNFs, it can be distinctly seen that the peak current intensity increase with the square root of scanning rate, while the oxidation peaks and reduction peaks move to more positive and negative values, respectively. These results indicate that the diffusion resistance raises with the increase of scanning speed. Figure 14 b–f give the charge-discharge behavior of the three electrodes between 0.0 and 0.53 V at different current densities (from 0.5 to 5 A g⁻¹). In the meantime, these representative voltage plateaus are in well agreement with the peaks observed in CV curves. At the current density of 5 A g⁻¹, the capacitance of the Sn/C sample still keeps 559.51 F g⁻¹. Obviously, the as-obtained Sn/C sample has a potential application value as the electrode material for supercapacitors.

The rate performance, which straightly relies on the capacitance reduction observed in GCD measurements, is shown in Fig. 15. When the current density is 0.5 A g⁻¹, the specific capacitance of Sn/CNFs is

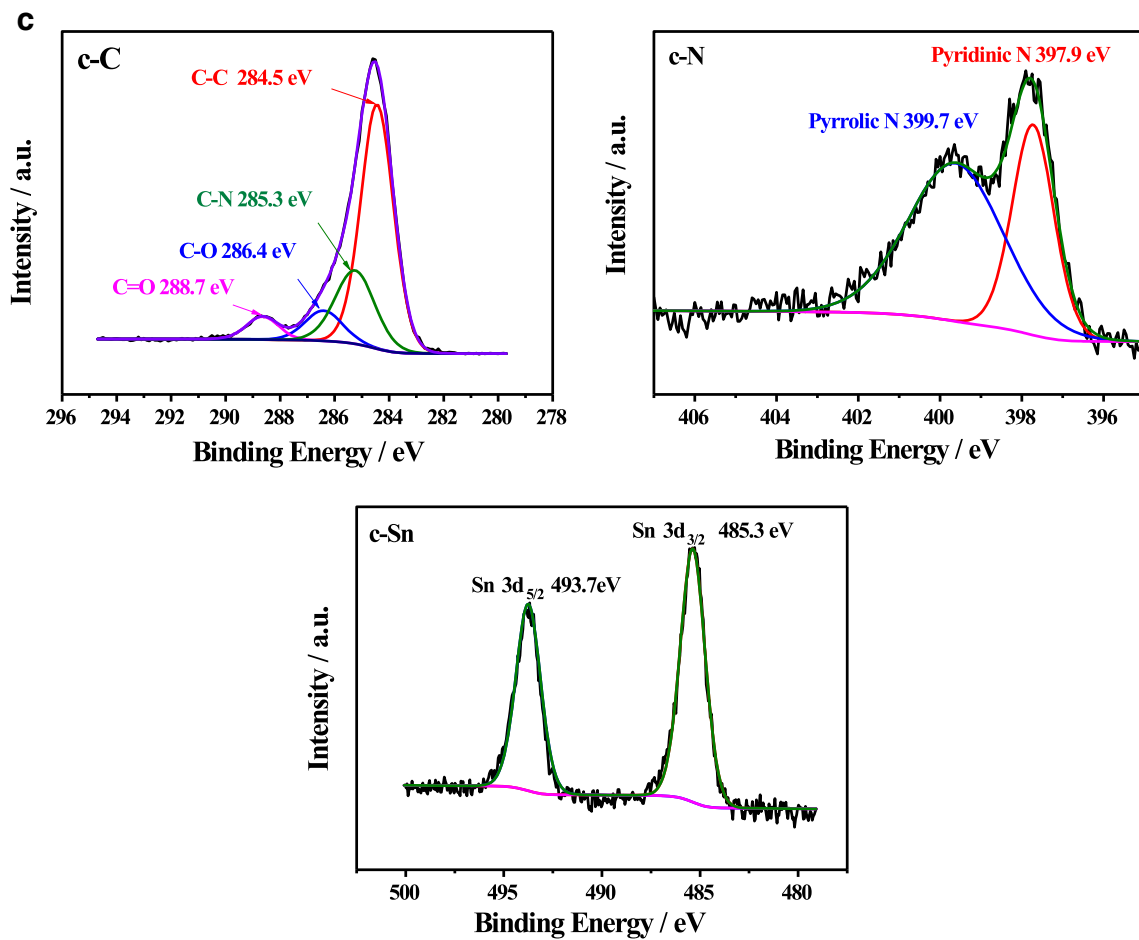


Fig. 6 (continued)

calculated as 761.39 F g^{-1} , which is greater than those of Sn/SnO/CNFs and SnO₂/CNFs (712.29 F g^{-1} , 589.78 F g^{-1}). Simultaneously, it should be noted that, at a high current density of 5 A g^{-1} , the specific capacitance of Sn/CNFs is 579.51 F g^{-1} , which is 76.11% of that at 0.5 A g^{-1} . For SnO₂/CNFs and Sn/SnO/CNFs, the corresponding values are only 429.38 and 528.12 F g^{-1} at 5 A g^{-1} , and the capacitance retentions

are 74.14% and 72.80%, respectively, indicating that the Sn/CNFs exhibits good rate capability.

To further support for this electrochemical behavior, three samples are tested by electrochemical impedance spectroscopy (EIS) in the frequency range of 100 to 0.01 KHz. Figure 16a and b display the Nyquist plot of the SnO₂/CNFs, Sn/SnO/CNFs, and Sn/CNFs composite materials at open circuit potential. The series

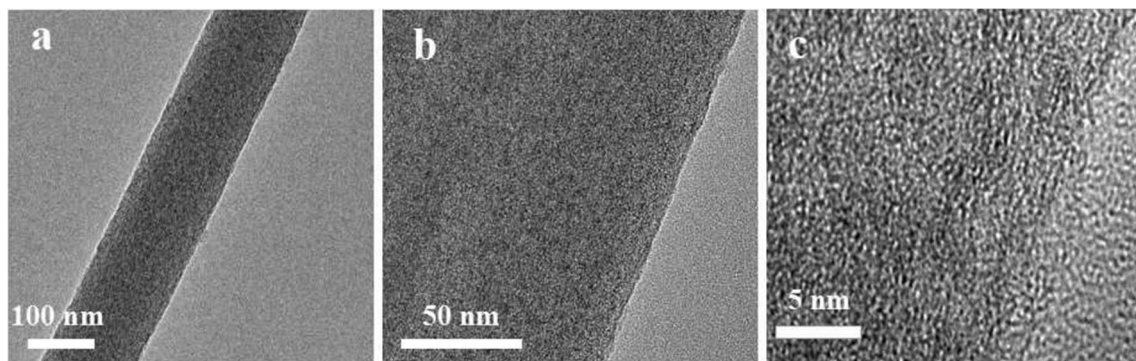
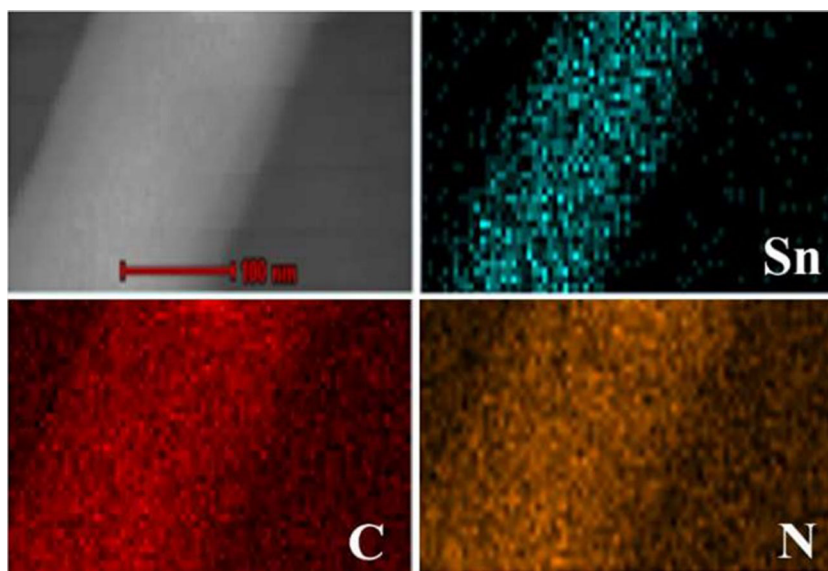


Fig. 7 (a and b) TEM and (c) HR-TEM images of the Sn/CNFs

Fig. 8 Elemental mapping images of Sn/CNFs



resistance (R_s) of SnO₂/CNFs, Sn/SnO/CNFs, and Sn/CNFs is 0.45, 0.42, and 0.38 Ω , respectively. Resistance mainly comes from bulk solution, electrode resistance, and ion diffusion resistance [44]. It is observed that there is no semicircle in the high frequency range of impedance indicating that the charge transfer resistance is small. This can be explained by the uniform distribution of tin on nanofibers, which increases the conductivity of the electrodes and reduces the intrinsic resistance of the nanofibers [37]. Therefore, the electrochemical performance of Sn/CNFs is better than that of SnO₂/CNFs and Sn/SnO/CNFs.

The long-term cycling property is a significant argument for evaluating the performance of supercapacitors and electrodes. Accordingly, SnO₂/CNFs, Sn/SnO/CNFs, and Sn/CNFs circulate 10,000 times at the current density of 5 A g⁻¹ as shown in Fig. 17. In this case, the

final specific retentions of SnO₂/CNFs, Sn/SnO/CNFs, and Sn/CNFs were about 106.46%, 112.43%, and 114.05%. It is noteworthy that the capacitance of Sn/CNFs electrodes continues to increase in the initial cycle, which may be due to the fact that only part of the material is active in the initial cycle. In the subsequent cycle, the electrolyte (OH⁻) gradually penetrates into the surface-constrained nanomaterials, pushing the capacitance and conductivity to a higher level and keeping the capacitance and peak current basically unchanged. In this process, due to the insertion and layering of ions in the cycle, the electrode material will be fully activated and the electrolyte will be completely immersed in the electrode surface, which is conducive to the electrochemical intercalation/delamination of ions and makes the redox reaction of the whole surface simpler. Up to 4800 cycles, the capacitance of Sn/CNFs electrode achieved the

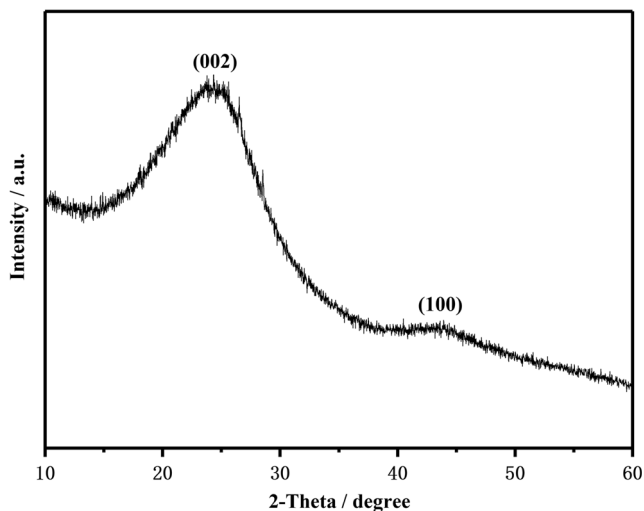


Fig. 9 XRD spectra of Sn/CNFs

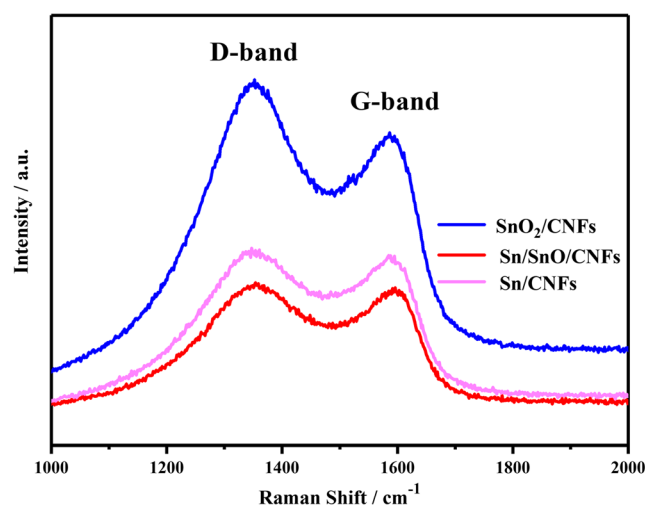


Fig. 10 Raman spectra of SnO₂/CNFs, Sn/SnO/CNFs, and Sn/CNFs

Table 1 Specific surface area of the SnO₂/CNFs, Sn/SnO/CNFs, and Sn/CNFs

Samples	SnO ₂ /CNFs	Sn/SnO/CNFs	Sn/CNFs
S _{BET} (m ² /g)	20.27	23.62	24.65

maximal value and the capacitance conservation rate is 123%. The capacitance diminished in the last several cycles could be attributed to the mild structure degradation induced by the repetition of ion intercalation/deintercalation [45].

In order to further prove the practical application potential of Sn/CNFs nanomaterials, an asymmetric supercapacitor was assembled with Sn/CNFs as positive electrode and CNFs-700 as negative electrode. The two electrodes have different voltage windows for CNFs (−0.9–0 V) and Sn/CNFs (0–0.65 V), so the voltage of Sn/CNFs//CNFs asymmetric supercapacitor can reach 1.5 V (Fig. 18a), widening the voltage window of single electrode. It is observed from the figure that, when the scanning rate increases from 2 to 50 mv s^{−1}, the CV curve of Sn/CNFs//CNFs does not have a large deformation, which proves that the two-electrode system has good

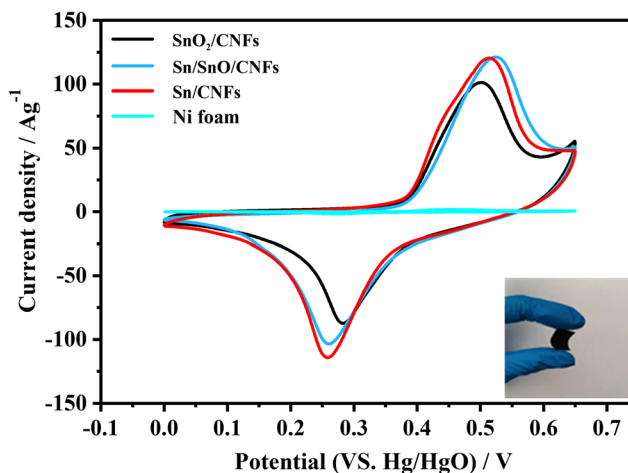


Fig. 12 CV curves of SnO₂/CNFs, Sn/SnO/CNFs, Sn/CNFs, and Nickel foam at a scan rate of 70 mV s^{−1}

reversibility. The electrochemical performance of asymmetric supercapacitors at different current densities is further evaluated by GCD, as shown in Fig. 18b. The specific capacitance of Sn-CNFs//CNFs was calculated according to the total mass of the positive and negative electrode materials. When the current densities are 0.5, 0.8, 1, 2,

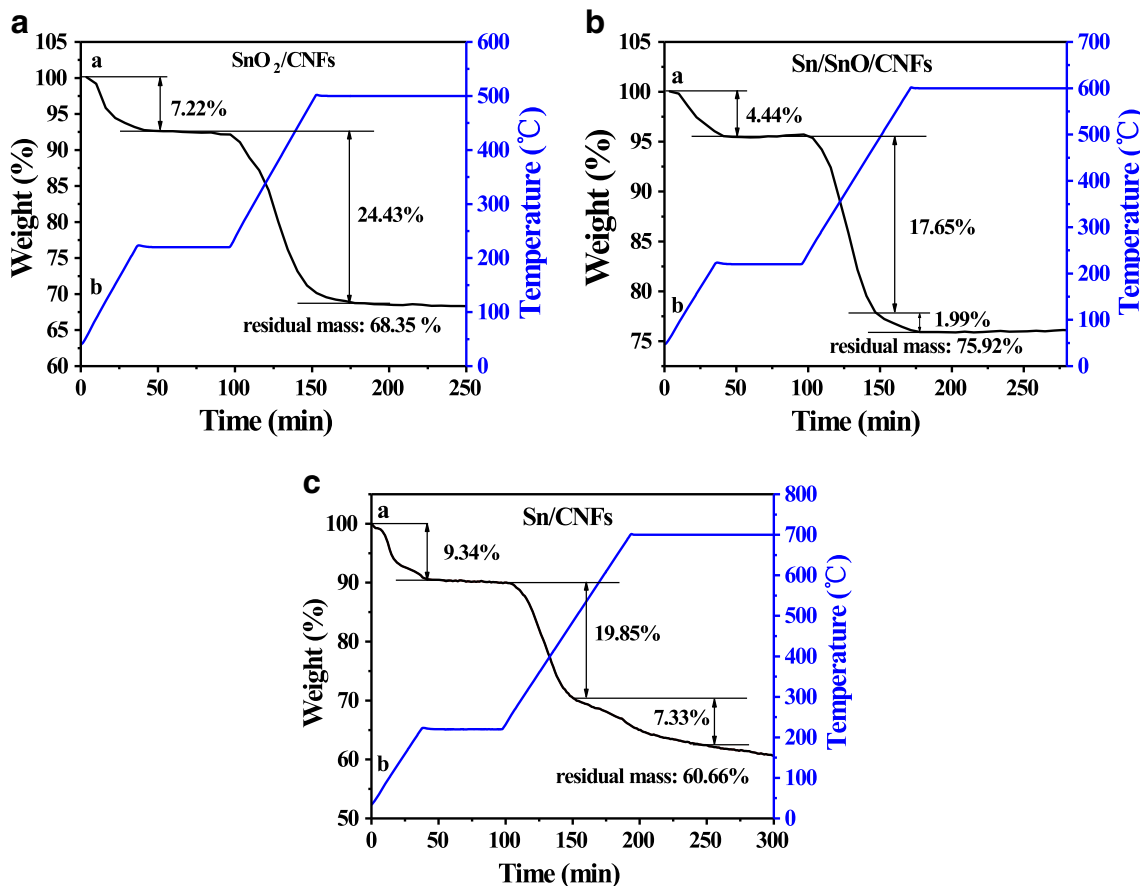


Fig. 11 TGA thermograms of SnO₂/CNFs (a), Sn/SnO/CNFs (b), and Sn/CNFs (c); TG curve of samples (a) and present temperature program (b)

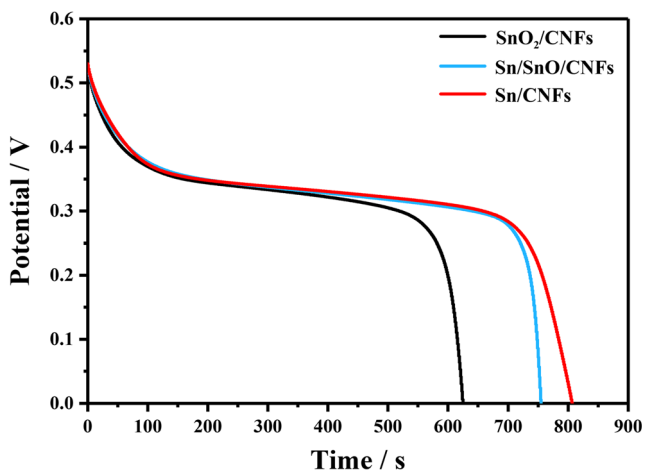


Fig. 13 Charge and discharge curves of SnO₂/CNFs, Sn/SnO/CNFs, Sn/CNFs at a current density of 0.5 A g⁻¹

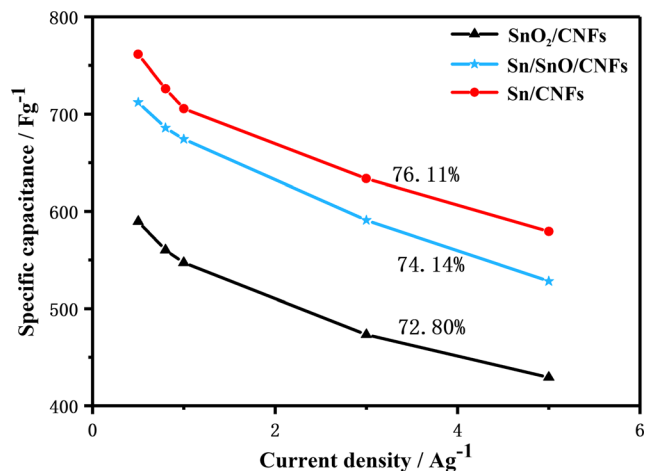
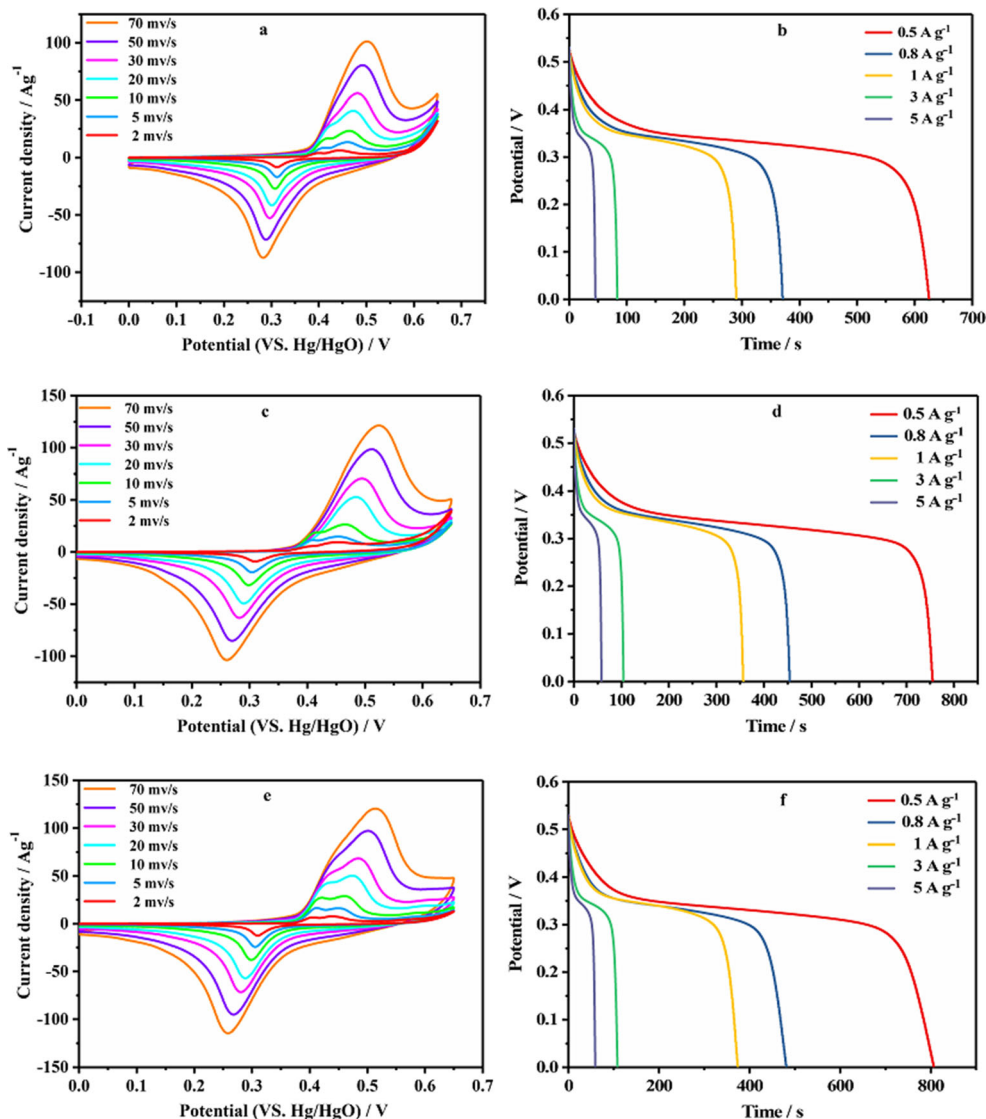


Fig. 15 Specific capacitance of SnO₂/CNFs, Sn/SnO/CNFs, Sn/CNFs at different current densities

Fig. 14 (a) CV curves of SnO₂/CNFs at the scan rates from 2 to 70 mv s⁻¹. (b) Charge and discharge curves of SnO₂/CNFs at the current density of 0.5–5 A g⁻¹. (c) CV curves of Sn/SnO/CNFs at the scan rates from 2 to 70 mv s⁻¹. (d) Charge and discharge curves of Sn/SnO/CNFs at the current density of 0.5–5 A g⁻¹. (e) CV curves of Sn/CNFs at the scan rates from 2 to 70 mv s⁻¹. (f) Charge and discharge curves of Sn/CNFs at the current density of 0.5–5 A g⁻¹



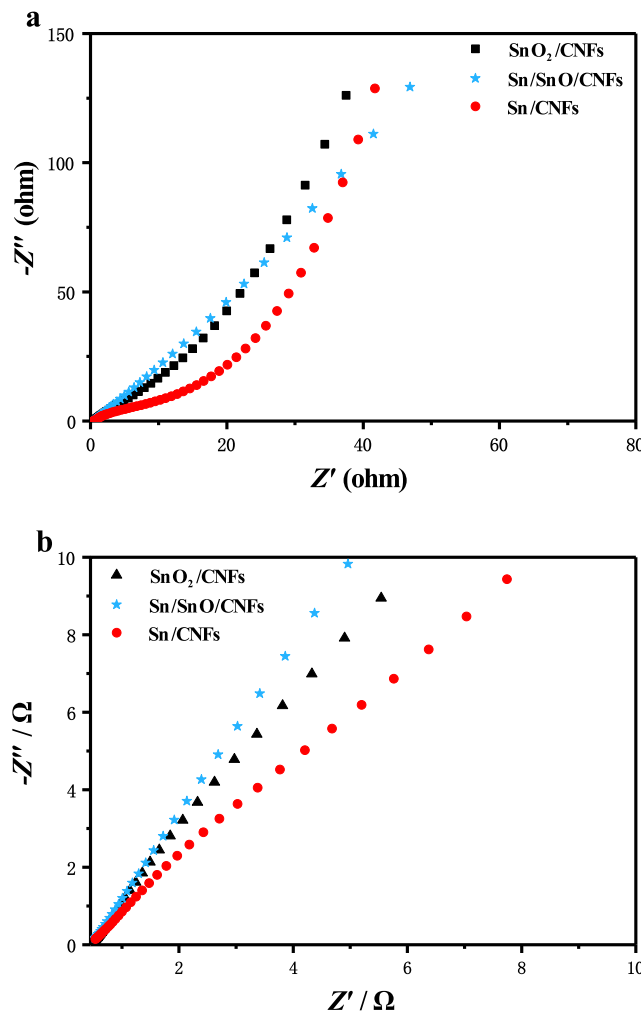


Fig. 16 (a) Nyquist plots of SnO₂/CNFs, Sn/SnO/CNFs, Sn/CNFs, (b) magnified version of the Nyquist plots

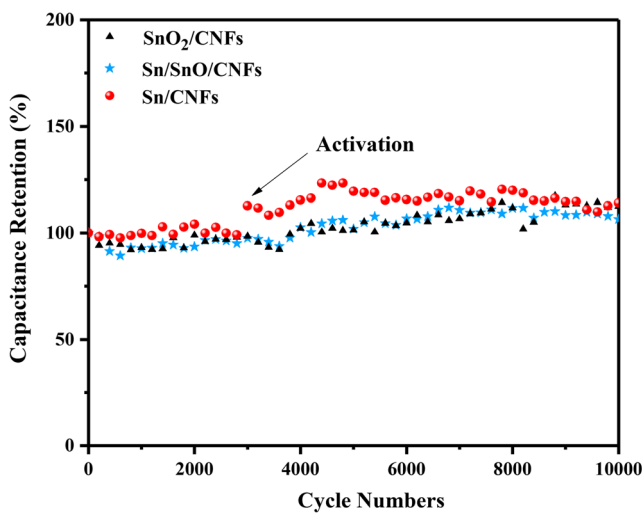


Fig. 17 Cycling performances of the SnO₂/CNFs, Sn/SnO/CNFs, and Sn/CNFs at a current density of 5 A g⁻¹

and 3 A g⁻¹, the specific capacitances of asymmetric supercapacitors are 182.9, 155.7, 143.9, 101.2, and 100.8 F g⁻¹, respectively. From the results, it can be seen that the specific capacitance decreases with the increase of current density, which is caused by the decrease of utilization ratio of active materials and the limitation of ion diffusion/migration. It is well known that, under the premise of high power density, high energy density is an important parameter of a good supercapacitor. Figure 18 d shows the Ragone plot of energy and power density at different current densities and compares them with literatures. When the power density changes from 3748.8–374.9 W kg⁻¹, the energy density varies from 25.9 to 57.2 Wh kg⁻¹. Recent reports, such as 11.2 Wh kg⁻¹ and 923.1 W kg⁻¹ for the PC/KOH/Cu₅Sn₂S₇/ZnS supercapacitor [46], 23 Wh kg⁻¹ and 90 W kg⁻¹ for the Co₂SnO₄ nanocubes [47], and 36 Wh kg⁻¹ and 1440 W kg⁻¹ for the Sn-Gr electrode materials [48]. All these excellent results demonstrate the promising potential of the Sn-CNFs//CNFs for supercapacitor applications.

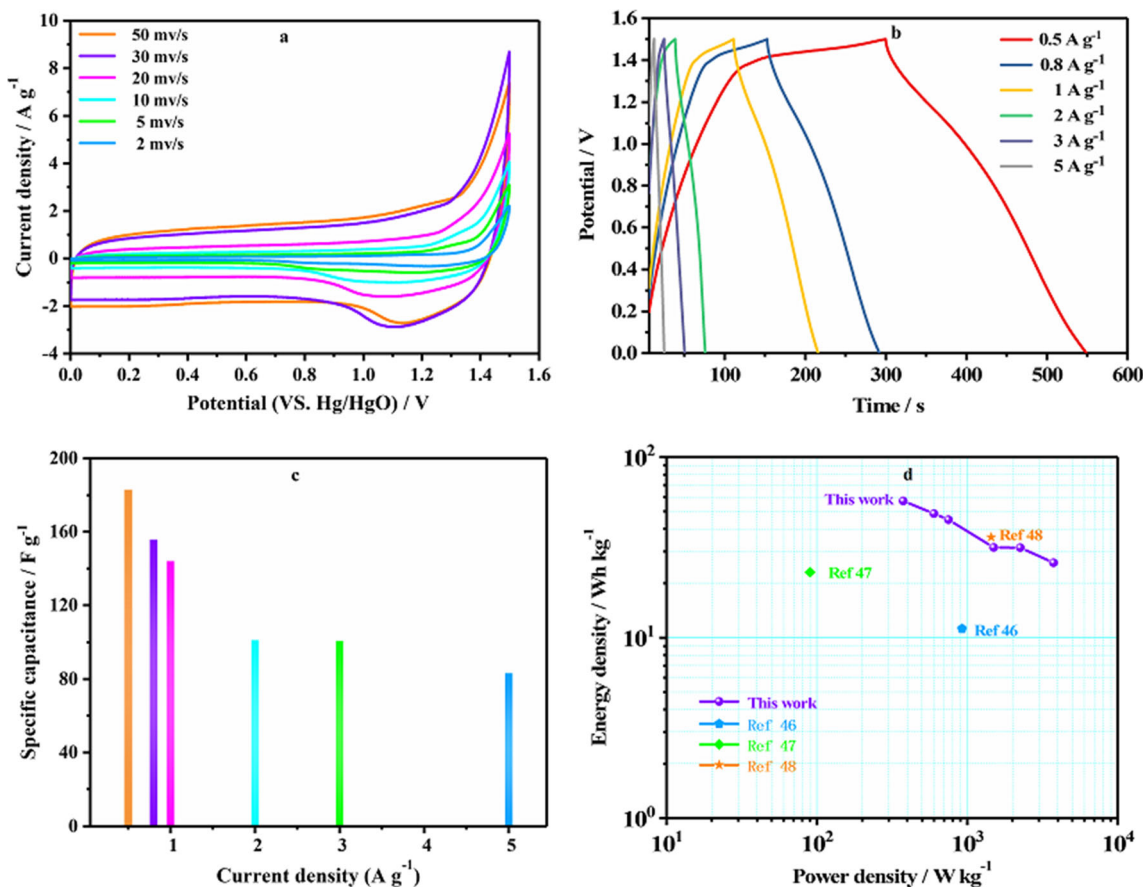


Fig. 18 (a) CV curves at different scan rates of the Sn/CNFs//CNFs asymmetric supercapacitor. (b) Charge and discharge curves of Sn/CNFs//CNFs asymmetric supercapacitor at the current density of 0.5–5 A g⁻¹. (c) Effects of the current density on the specific capacitance of

Sn/CNFs//CNFs asymmetric supercapacitor. (d) Ragone plots of Sn/CNFs//CNFs asymmetric supercapacitor and some other hybrid materials reported in the literatures

Conclusions

In summary, we systematically investigated the optimum status of Sn-embedded carbon nanofibers applied to electrode materials of supercapacitors, including the optimum ratio of SnCl₂ to PAN and the optimum valence state of tin. When the molar ratio of AN/SnCl₂ is 40/1, the optimized specific capacitance of SnO_x/CNFs (40) is 589.78 F g⁻¹ at 0.5 A g⁻¹. Afterwards, Sn/CNFs, Sn/SnO/CNFs, and SnO₂/CNFs were prepared by different carbonization processes at the optimum ratio. The specific capacitance at 0.5 A g⁻¹ is 761.39 F g⁻¹, 712.29 F g⁻¹, and 587.78 F g⁻¹, respectively. In addition, Sn/C nanofibers remained stable after 10,000 cycles and maintained 114% of their initial properties. To further estimate the Sn/C electrode for practical application, the Sn/C as the positive electrode and CNFs-700 as negative electrode were assembled into the asymmetric supercapacitor (ASC). The resulting Sn-CNFs//CNFs device represented maximum energy density of 57.18 Wh kg⁻¹ at the power density of 375 W kg⁻¹. Therefore, this study not only provides a strategy for the synthesis of tin-embedded composites with different valence states of carbon

nanofibers but also shows that Sn/CNFs is a potential electrode material for supercapacitors.

Funding information The authors gratefully acknowledge the support from the National Natural Science Foundation of China (No. 21766022).

References

- Shao Z, Qi H, Wang X, Sun J (2019) Boosting oxygen evolution by surface nitrogen doping and oxygen vacancies in hierarchical NiCo/NiCoP hybrid nanocomposite. *Electrochim Acta* 296:259–267
- Sun J, Guo N, Shao Z (2018) A facile strategy to construct amorphous spinel-based electrocatalysts with massive oxygen vacancies using ionic liquid dopant. *Adv Energy Mater* 8:1800980
- Zhang L, Zhao X (2009) Carbon-based materials as supercapacitor electrodes. *Chem Soc Rev* 38:2520–2531
- Yu M, Huang Y, Li C, Zeng Y, Wang W, Li Y (2015) Building three-dimensional graphene frameworks for energy storage and catalysis. *Adv Funct Mater* 25:324–330
- Mayer S, Pekala R, Kaschmitter J (1993) The aerocapacitor: an electrochemical double-layer energy-storage device. *J Electrochem Soc* 140:446–451

6. Chen X, Zhao B, Cai Y, Tade M, Shao Z (2013) Amorphous V–O–C composite nanofibers electrospun from solution precursors as binder- and conductive additive-free electrodes for supercapacitors with outstanding performance. *Nanoscale* 5:12589–12597
7. L. Chen, X. Zhang, H. Liang, M. Kong, Q. Guan, P. Chen, (2013) *ACS Nano* 6:7092–7102
8. Zhang Y, Hu Z, Liang Y, Yang Y, An N, Li Z (2015) Growth of 3D SnO₂ nanosheets on carbon cloth as a binder-free electrode for supercapacitors. *J Mater Chem A* 3:15057–15067
9. Ji L, Lin Z, Guo B, Medford A (2010) Assembly of carbon-SnO₂ core-sheath composite nanofibers for superior lithium storage. *Chem Eur J* 16:11543–11548
10. Samuel E, Joshi B, Jo H, Kim Y, Swihart M, Yun J (2017) Flexible and freestanding core-shell SnO /carbon nanofiber mats for high-performance supercapacitors. *J. Alloy. Compd.* 728:1362–1371
11. Maier J (2013) Thermodynamics of electrochemical lithium storage. *Angew Chem Int Ed* 52:4998–5026
12. Ding W, Li L, Zhang L, Ju D, Peng S, Chai W (2013) An XPS study on the chemical bond structure at the interface between SiO_xN_y and N doped polyethylene terephthalate. *J Chem Phys* 138:104706
13. Goodenough J, Kim Y (2010) Challenges for rechargeable Li batteries†. *Chem Mater* 22:587–603
14. Kim C, Yang K, Kojima M, Yoshida K, Kim Y, Kim Y (2006) Fabrication of electrospinning-derived carbon nanofiber webs for the anode material of lithium-ion secondary batteries. *Adv Funct Mater* 16:2393–2397
15. Kim M, Cho J (2009) Reversible and high-capacity nanostructured electrode materials for Li-ion batteries. *Adv Funct Mater* 19:1497–1514
16. Kong J, Liu Z, Yang Z, Tan H, Xiong S, Wong S (2012) Carbon/SnO₂/carbon core/shell/shell hybrid nanofibers: tailored nanostructure for the anode of lithium ion batteries with high reversibility and rate capacity. *Nanoscale* 4:525–530
17. Li H, Huang X, Chen L (1999) Electrochemical impedance spectroscopy study of SnO and nano-SnO anodes in lithium rechargeable batteries. *J Power Sources* 81–82:340–345
18. Zhao M, Zhao Q, Qiu J, Xue H, Pang H (2016) Tin-based nanomaterials for electrochemical energy storage. *RSC Adv* 6: 95449–95468
19. Joshi B, An S, Kim Y, Samuel E, Song K, Seong I (2007) Preparation of Fe–C nanofiber composites by metal organic complex and potential application in supercapacitors. *J Alloy Compd* 700:259–266
20. Aldon L, Garcia A, Olivier-Fourcade J, Jumas J, Fernández-Madriral F, Lavela P (2003) Lithium insertion mechanism in Sb-based electrode materials from 121Sb Mössbauer spectrometry. *J Power Sources* 119–121:585–590
21. Beaulieu L, Eberman K, Turner R, Krause L, Dahn J (2001) Colossal reversible volume changes in lithium alloys. *Electrochem Solid-State Lett* 4:A137–A140
22. Beaulieu L, Hatchard T, Bonakdarpour A, Fleischauer M (2003) Reaction of Li with alloy thin films studied by in situ AFM. *J Electrochem Soc* 150:A1457–A1464
23. Mu J, Chen B, Guo Z, Zhang M, Zhang Z, Shao C (2011) Tin oxide (SnO₂) nanoparticles/electrospun carbon nanofibers (CNFs) heterostructures: controlled fabrication and high capacitive behavior. *J Colloid Interface Sci* 356:706–712
24. Wang W, Lei W, Yao T, Xia X, Huang W, Hao Q (2013) One-pot synthesis of graphene/SnO₂/PEDOT ternary electrode material for supercapacitors. *Electrochim Acta* 108:118–126
25. Hao S, Sun Y, Liu Y, Zhang Y, Hu G (2016) Facile synthesis of porous SnO₂ film grown on Ni foam applied for high-performance supercapacitors. *J. Alloy. Compd.* 689:587–592
26. Yan Z, Qi H, Bai X (2018) Mn doping of cobalt oxynitride coupled with N-rGO nanosheets hybrid as a highly efficient electrocatalyst for oxygen reduction and oxygen evolution reaction. *Electrochim Acta* 283:548–559
27. Huang J, Zhang B, Xie Y, Lye W, Xu Z, Abouali S (2016) Electrospun graphitic carbon nanofibers with in-situ encapsulated Co–Ni nanoparticles as freestanding electrodes for Li–O₂ batteries. *Carbon* 100:329–336
28. Li B, Ge X, Goh FT, Hor TA, Geng D, Du G (2015) Co₃O₄ nanoparticles decorated carbon nanofiber mat as binder-free air-cathode for high performance rechargeable zinc-air batteries. *Nanoscale* 7:1830–1838
29. Meng F, Zhong H, Bao D, Yan J, Zhang X (2016) In situ coupling of strung Co₄N and intertwined N–C fibers toward free-standing bifunctional cathode for robust, efficient, and flexible Zn–air batteries. *J Am Chem Soc* 138:10226–10231
30. Wang Z, Peng S, Hu Y, Li L, Yan T, Yang G (2017) Cobalt nanoparticles encapsulated in carbon nanotube-grafted nitrogen and sulfur co-doped multichannel carbon fibers as efficient bifunctional oxygen electrocatalysts. *J Mater Chem A* 5:4949–4961
31. Zhao K, Xu Z, He Z, Ye G, Gan Q, Zhou Z (2018) Vertically aligned MnO₂ nanosheets coupled with carbon nanosheets derived from Mn-MOF nanosheets for supercapacitor electrodes. *J Mater Sci* 53:13111–13125
32. Kumar M, Yun J, Bhatt V, Singh B, Kim J, Kim J (2018) Role of Ce³⁺ valence state and surface oxygen vacancies on enhanced electrochemical performance of single step solvothermally synthesized CeO₂ nanoparticles. *Electrochim Acta* 284:709–720
33. Ki S, Lee H, Park Y, Kim S, An K, Jung S (2018) Assessing the electrochemical performance of a supercapacitor electrode made of copper oxide and activated carbon using liquid phase plasma. *Appl Surf Sci* 446:243–249
34. Huang G, Li C, Sun X, Bai J (2017) Fabrication of vanadium oxide, with different valences of vanadium, -embedded carbon fibers and their electrochemical performance for supercapacitor. *New J Chem* 41:8977–8984
35. Yu M, Zeng Y, Han Y, Cheng X, Zhao W, Liang C (2015) Valence-optimized vanadium oxide supercapacitor electrodes exhibit ultrahigh capacitance and super-long cyclic durability of 100 000 cycles. *Adv Funct Mater* 25:3534–3540
36. Wang H, Huang H, Chen L, Wang C, Yan B, Yu Y (2014) Preparation of Si/Sn-based nanoparticles composited with carbon fibers and improved electrochemical performance as anode materials. *ACS Sustain Chem Eng* 2:2310–2317
37. Mao M, Yan F, Cui C, Ma J, Zhang M, Wang T (2017) Pipe-wire TiO₂–Sn@Carbon nanofibers paper anodes for lithium and sodium ion batteries. *Nano Lett* 17:3830–3836
38. Bai X, Wang Q (2017) Phosphorus and fluorine co-doping induced enhancement of oxygen evolution reaction in bimetallic nitride nanorods arrays: ionic liquid-driven and mechanism clarification. *Chem Eur J* 23:16862–16870
39. Guo H, Zhao H, Yin C, Qiu W (2006) Si/SnSb alloy composite as high capacity anode materials for Li-ion batteries. *J Alloy Compd* 426:277–280
40. Yu Q, Guan D, Zhang Z (2017) Mass production of monodisperse carbon microspheres with size-dependent supercapacitor performance via aqueous self-catalyzed polymerization. *ChemPlusChem* 82(6):872–878
41. Zhuo K, Jeong M, Shin M, Chun W, Bae J, Yoo P (2014) Morphological variation of highly porous Ni–Sn foams fabricated by electro-deposition in hydrogen-bubble templates and their performance as pseudo-capacitors. *Appl Surf Sci* 322:15–20
42. Thorat M, Jadhav S (2018) Collective use of deep eutectic solvent for one-pot synthesis of ternary Sn/SnO₂@C electrode for supercapacitor. *J. Alloy. Compd.* 732:694–704
43. Meng X, Zhou M (2013) Synthesis of SnO₂ nanoflowers and electrochemical properties of Ni/SnO₂ nanoflowers in supercapacitor. *Electrochim Acta* 109:20–26

44. Zhang X, Shi W, Zhu J, Kharistal D, Zhao W (2011) High-power and high-energy-density flexible pseudocapacitor electrodes made from porous CuO nanobelts and single-walled carbon nanotubes. *ACS Nano* 5:2013–2019
45. Cui X, Hu F, Wei W, Chen W (2011) Dense and long carbon nanotube arrays decorated with Mn₃O₄ nanoparticles for electrodes of electrochemical supercapacitors. *Carbon* 49:1225–1234
46. Yu F, Pang L (2019) Flower-like Cu₅Sn₂S₇/ZnS nanocomposite for high performance supercapacitor. *Chinese Chem Lett.* <https://doi.org/10.1016/j.ccl.2019.01.004>
47. Raj BGS, Bhuvaneshwari S, Wu JJ, Asiri AM, Anandan S (2018) Sonochemical synthesis of Co₂SnO₄ nanocubes for supercapacitor applications. *Ultrason Sonochem* 41:435–440
48. Qin Z, Li Z (2012) Sn nanoparticles grown on graphene for enhanced electrochemical properties. *J Power Sources* 217:303–308

Publisher's note Springer Nature remains neutral with regard to jurisdictional claims in published maps and institutional affiliations.